JOURNAL OF THE AMERICAN CHEMICAL SOCIETY

pubs.acs.org/JACS Article

Strong Structural and Electronic Coupling in Metavalent PbS Moiré Superlattices

Yu Wang,[#] Zhigang Song,[#] Jiawei Wan, Sophia Betzler, Yujun Xie, Colin Ophus, Karen C. Bustillo, Peter Ercius, Lin-Wang Wang, and Haimei Zheng*

Cite This: *J. Am. Chem. Soc.* 2022, 144, 23474−23482 Read Online

ACCESS | Metrics & More | Article Recommendations | Supporting Information

ABSTRACT: Moiré superlattices are twisted bilayer materials in which the tunable interlayer quantum confinement offers access to new physics and novel device functionalities. Previously, moiré superlattices were built exclusively using materials with weak van der Waals interactions, and synthesizing moiré superlattices with strong interlayer chemical bonding was considered to be impractical. Here, using lead sulfide (PbS) as an example, we report a strategy for synthesizing moiré superlattices coupled by strong chemical bonding. We use water-soluble ligands as a removable template to obtain free-standing ultrathin PbS nanosheets and assemble them into direct-contact bilayers with various twist angles. Atomic-resolution imaging shows the moiré periodic structural reconstruction at the superlattice interface due to the strong metavalent coupling. Electron energy loss spectroscopy and theoretical calculations collectively reveal the twist-angle-dependent electronic structure, especially the emergent separation of flat bands at small twist angles. The localized states of flat bands are similar to well-arranged quantum dots, promising an application in devices. This study opens a new door to the exploration of deep energy modulations within moiré superlattices alternative to van der Waals twistronics.

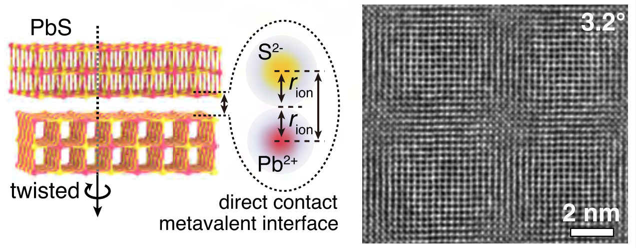

■ INTRODUCTION

Recently, moiré superlattices have been synthesized by stacking two layers of two-dimensional (2D) materials with relative twist angles,[1,2] in which the long-range superlattice potentials from interlayer interactions can create quantum confinement in each layer. Quantum confinement in moiré superlattices can slow down or localize electrons, providing a tunable platform for studying strongly correlated physics,[3,4] such as superconductivity,[1,5] Mott insulators,[6] and interacting topological insulators.[7,8] In the moiré superlattices, the twisting topology determines the 2D quantum confinement, and it offers an additional degree of freedom to modulate the electronic structure, usually termed twistronics.[9,10] To date, all 2D moiré superlattices have been synthesized using van der Waals (vdW) materials,[11] such as graphene and transition metal dichalcogenides, where the two layers of materials are coupled through vdW interactions. Twistronics based on these vdW materials has attracted great interest in various fields, ranging from physics[12−19] to materials science[20−23] and chemistry.[24,25] Different from materials coupled by chemical bonding at an interface, such as conventional semiconductor heterostructures, vdW twistronics have reduced strength in modulating the electronic structures due to the weak interlayer coupling, although strong coupling in twistronics is desired.[26,27] Most of the experimental observations of exotic electronic properties, especially those associated with electron transport, are realized at extremely low temperatures.[3,4,6−8,28] To increase the electronic modulation imposed by the moiré superlattice, one approach is to replace the vdW interactions with strong chemical bonding such as covalent, ionic, or metavalent bonding.

Achieving strong quantum confinement in moiré superlattices by chemical bonding will pave a way to the fabrication of a new class of materials for beyond-vdW twistronics,[29] and it may also shed light on some challenging issues in other systems. For example, strongly coupled moiré superlattices can be structurally and functionally similar to an array of quantum dots,[30] offering an alternative route to supercrystals[31] by avoiding the notorious issue of connection defects formed during quantum dot self-assembly.[32] Moreover, the energy bands near the Fermi level in moiré patterns can be flattened due to the strong modulation, which may trap electrons in individual “quantum-dot” potentials upon suitable doping, leading to Wigner crystallization.[33−35] Thus, creating strongly coupled moiré superlattices through chemical bonding

Received: September 18, 2022
Published: December 13, 2022

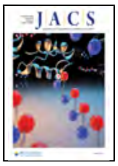

https://doi.org/10.1021/jacs.2c09947

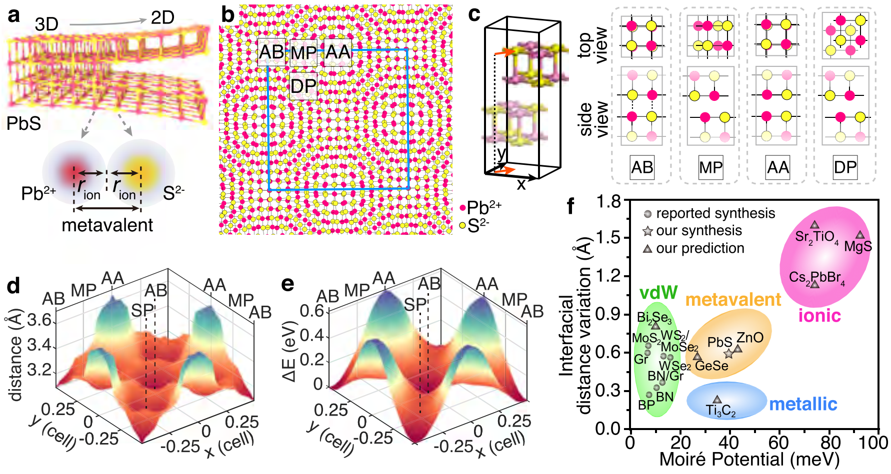

Figure 1. Structure and strong coupling of PbS moiré superlattices. (a) 3D and cleaved 2D structures of PbS rock-salt crystal, emphasizing the metavalent interaction in all directions. (b) Different local atomic alignments occur in a PbS moiré superlattice with a twist angle of 8°. The blue square marks the moiré unit cell. Four representative stacking configurations are highlighted as Pb on Pb (AA), Pb on S (AB), middle point (MP), and diagonal point (DP). (c) Illustration of lateral shifting of two PbS nanosheets to create different stacking configurations. Top and side views of representative structures are shown. (d, e) DFT calculations of the structures created according to (c), showing the interfacial distance (d) and the free energy change (e) upon the bilayer lateral shift. (f) DFT calculations on varieties of moiré superlattices, including the reported vdW superlattices, the metavalent PbS synthesized in this work, and our predictions of other chemically bonded superlattices. The results show their moiré potential and the largest interfacial distance variation among different stacking configurations.

combines the strengths of two fields: the tunable confinement of 2D moiré superlattices and the strong coupling in conventional semiconductor heterostructures.

Despite their promising unique features, chemically bonded moiré superlattices are unexplored due to the difficulty of synthesis. Having chemical bonding at moiré interfaces means that the materials are nonlayered with intrinsically 3D crystalline structures, such as metals, II−VI semiconductors, and perovskites. Colloidal synthesis is a most important and common strategy to fabricate 2D nanocrystals with great material and structural versatility. It is natural to think assembling colloidally synthesized 2D nanocrystals into chemically bonded superlattices. However, this requires a challenging ligand removal process, as ligands of 2D nanocrystals are principally designed to ligate strongly to guide asymmetric growth and stabilize the formed nanocrystals.

Here we use PbS as a model system to demonstrate a colloidal synthesis strategy for constructing chemically bonded moiré superlattices through the subtle design of removable ligands. Such beyond-vdW moiré superlattices are synthesized and examined for the first time. Strong interfacial coupling of the superlattice is revealed through atomic-resolution imaging, and the giant electronic modulation of the moiré pattern is validated through the combination of electron energy loss spectroscopic analysis and theoretical calculations.

■ RESULTS AND DISCUSSION

Conceptual Discussion of Metavalent Moiré Superlattices. We first describe theoretically why chemically bonded moiré superlattices can give rise to stronger coupling effects than vdW moiré superlattices. As shown in Figure 1a, bulk PbS has a rock-salt crystal structure and features an unconventional type of chemical bonding between Pb and S atoms, namely, metavalent bonding. This term was created by theorists to specifically describe the fundamental bonding mechanisms of metal chalcogenides such as PbS, PbSe, and SnTe: the valence electrons in metavalent bonding are delocalized to an extent between covalent and ionic bonding.[25] This metavalent Pb−S bonding is much stronger than vdW interactions,[20] and it can be used as the interlayer interaction to construct strongly coupled PbS moiré superlattices if one can assemble ultrathin 2D PbS nanosheets with pristine surfaces into twisted bilayers. This methodology may be further generalized to obtain new moiré superlattices coupled by other types of interfacial chemical bonding, for example, MXene[36] moiré superlattices coupled by metallic bonding, perovskite[37] moiré superlattices coupled by ionic bonding, and twisted bilayers of metal−organic frameworks[38] coupled by mixed interactions.

PbS moiré supercells with small commensurate angles have tetragonal symmetry (Figure 1b), in which two types of interfacial atoms stack into four general configurations: Pb on Pb (marked as AA), Pb on S (marked as AB), the middle point (MP) between AA and AB, and the diagonal point (DP) between two AB positions. In small-angle twisted bilayers, each stacking configuration can be approximated by small unit cells consisting of laterally shifted bilayers, in which the shift coordinates are scaled by x and y in the unit of cell size (Figure 1c). Therefore, the AB, AA, MP, and DP configurations correspond to $(x, y) = (0, 0)$, $(0, 0.5)$, $(0, 0.25)$, and $(0.25, 0.25)$, respectively, and other configurations between the four extrema can be constructed with continuous (x, y) shifts.

Density functional theory (DFT) calculations on the created structures (detailed in Supplementary Text S1) suggest that different stacking configurations can lead to deep modulations of interfacial reconstruction and electronic properties. Figure 1d,e shows the changes of interlayer distance and free energy as functions of lateral interlayer shift. The surface plot regarding either interlayer distance or free energy has the maxima at AA spots and the minima at AB spots. The difference between the maximum and minimum interlayer distance is as large as 0.6 Å, implying a possible structural reconstruction at the interface of a small-angle twisted superlattice.

The maximal free energy fluctuation in the real space is defined as the moiré potential,[16,39] which is an important indicator of the strength of energy modulation for a given moiré superlattice. We estimate the moiré potential of PbS and other 2D materials by calculating the largest free energy difference among all possible stacking configurations using approximate small unit cells. Figure 1f shows the calculated moiré potentials of various materials, including the reported vdW superlattices, the metavalent PbS synthesized in this work, and our predictions of other chemically bonded superlattices. The moiré potential of PbS is 40 meV/atom, more than twice those of the reported vdW superlattices. Generally, chemical bonding (e.g., metallic, metavalent, and ionic bonding) leads to much deeper energy modulation compared to vdW interactions. The deep energy modulation can localize electrons at the high-symmetry points with local energy extrema, providing an array of identical quantum-dot-like potentials.[30,31] Until now, the properties of the chemically bonded moiré superlattices and their structural stability remain unknown due to the lack of a synthesis strategy.

Synthesis of PbS Moiré Superlattices. Using metavalent PbS as a model system, we propose a colloidal synthesis strategy to construct chemically bonded moiré superlattices by employing moderately ligated and labile surfactant ligands. Strongly ligated ligands are typically necessary for guiding asymmetric growth during the colloidal synthesis of 2D nanocrystals. A commonly used ligand for synthesizing PbS nanocrystals is oleic acid, and removing it from the inorganic core has been a notorious problem in many related studies, e.g., full removal of oleic acid from quantum-dot surfaces is desired yet challenging.[40] Despite the previously reported synthesis of ultrathin PbS nanosheets,[41] ligands are present in their laminated structures and prevent direct contact of the PbS cores.

Analyzing the ligand chemistry (Figure 2a), we conjecture that the difficulty of removing oleic acid ligands comes from two aspects: (1) Ligand removal is required to occur in highly polar solvents (e.g., water) to break the Pb−carboxylate bonds and expose the highly polar PbS surfaces. However, oleic acid has low solubility in highly polar solvents due to its long alkyl chain. (2) The Pb−carboxylate bonding is relatively strong, as it is commonly used for building metal−organic frameworks.[42] To overcome this problem, we developed an aqueous synthesis strategy employing two surfactant ligands that have adequate solubility and bind moderately with the inorganic core. As shown in Figure 2b, dodecyl sulfate has a shorter alkyl chain and much better solubility in water compared with oleic acid. Our DFT calculations also indicate that dodecyl sulfate has a lower energy of bonding to PbS surface (0.347 eV) than does oleic acid (0.486 eV), suggesting an improved ligand leaving ability.

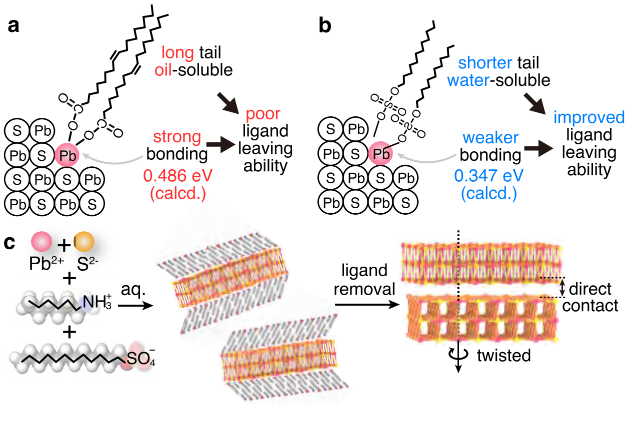

Figure 2. Synthesis of PbS moiré superlattices enabled by readily removable ligands. (a) Features and calculated surface bonding energy of a commonly used oil-soluble ligand, oleic acid, for colloidal synthesis of PbS nanocrystals. (b) As a comparison, water-soluble dodecyl sulfate ligand has a shorter chain and weaker surface bonding energy, improving the ligand leaving ability after aqueous colloidal synthesis. (c) Schematics of aqueous colloidal synthesis of PbS moiré superlattices.

Figure 2c shows the synthesis schematic (details are given in Supplementary Methods S1): Pb^{2+} and S^{2-} precursors and two water-soluble ligands (i.e., hexylamine and dodecyl sulfate) in an acidic aqueous solution at 80 °C for 20 min produce ligand-capped ultrathin PbS nanosheets. Then the ligands are readily removed by washing with dilute basic and acidic aqueous solutions alternately and rinsing with water. After ligand removal, the naked PbS nanosheets are immediately drop-cast, allowing the assembly of moiré superlattices through solvent evaporation.

Characterization of PbS Moiré Superlattices. TEM imaging and statistics (Figures 3a,b and S1) show that the nanosheets have a rectangular shape with average dimensions of around 40 nm × 200 nm. Aberration-corrected transmission electron microscopy (TEM) imaging (Figure 3c) and the zoomed-in portion from the yellow box (Figure 3d) with corresponding image simulation (Figure 3d inset) show that the as-synthesized nanosheets have a rock-salt structure with {001} surfaces and {110} edges. Energy-dispersive X-ray spectroscopy confirms that the moiré superlattice consists of Pb and S atoms in a molar ratio of 1:1 (Figure S2). We investigated the synthetic mechanism of PbS nanosheets by stopping the reaction earlier at 12 min and washing the product only twice with water. We observed the coexistence of PbS nanoparticles and nanosheets in the intermediate product, as shown in Figure S3. The size distribution of the nanoparticles was determined by image recognition and statistical analysis. Most of the nanoparticles have diameters of around 3 nm, approximately equal to the thickness of an individual nanosheet (characterized from side view, as shown in the next section). Further characterization of intermediate products at various reaction times (Figure S4) showed that small particles with a diameter of 2−4 nm appear at 2 min and then grow into platelets at 5 min. Fragmented sheets start to form after 8 min and grow into regular sheets in 20 min. Therefore, we conjecture that the aqueous synthesis of PbS nanosheets may undergo an oriented attachment process from nanoparticles to nanoplatelets and then to nanosheets. A similar oriented attachment route has been proposed for the synthesis of PbS nanosheets in organic solvents.[41]

After self-assembly, bilayer moiré superlattices with various twist angles are observed at low magnification due to the presence of moiré fringes (Figure 3e,f). A fast Fourier transform (FFT) of a representative moiré superlattice TEM image shows the expected pattern of two rotated sets of spatial frequencies corresponding to the structures of the individual sheets (Figure 3f). In the enlarged images (bottom panels of Figure 3f), the two red dots correspond to the (200) *d*-spacing of two individual sheets, the set of blue dots correspond to the *d*-spacings of the moiré pattern, and the orange dots correspond to the addition of the spatial frequencies from

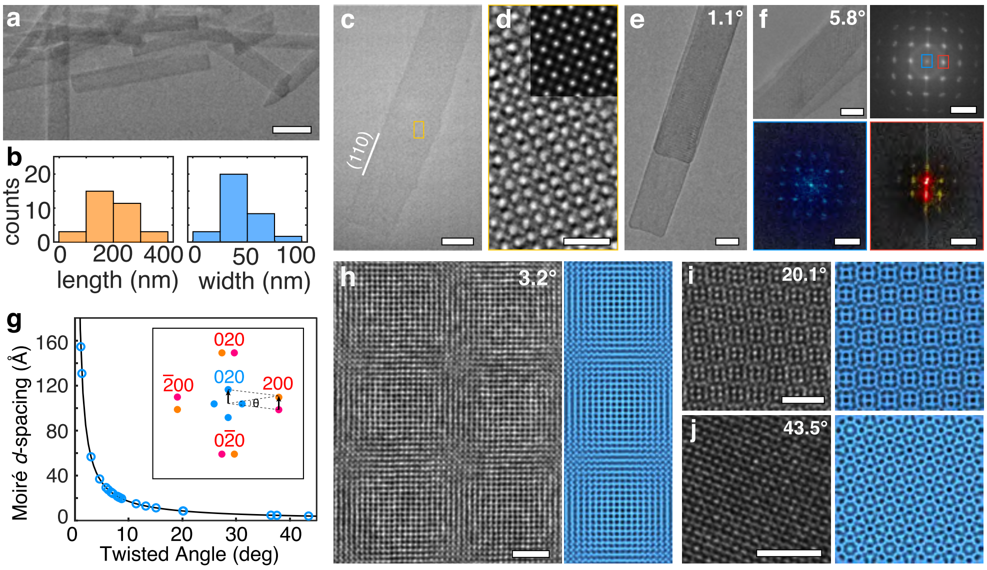

Figure 3. TEM characterizations of PbS moiré superlattices. (a) Representative TEM image of synthesized ultrathin PbS nanosheets. (b) Size distribution of PbS nanosheets obtained from analysis of (a) and Figure S1. (c) Low-magnification TEM image of a single PbS nanosheet. (d) Atomic-resolution image of the boxed area in (c). The inset shows a simulation of the TEM image. (e) TEM image of a bilayer moiré superlattice with a 1.1° twist angle. (f) TEM image (top left) and FFT pattern (top right) of a bilayer moiré superlattice with a 5.8° twist angle. The two bottom panels show the enlarged details of the FFT pattern, in which blue dots indicate moiré spatial frequencies, red dots indicate the (200) spatial frequencies of two individual rock-salt nanosheets, and orange dots indicate the merged pattern from the moiré pattern and individual rock-salt patterns. (g) Theoretical (black curve) and observed (green hollow dots) relationship between moiré *d*-spacing (200) and twist angles. The inset shows the relationship between moiré spatial frequencies (green) and two sets of individual rock-salt spatial frequencies (red and orange). (h−j) Atomic-resolution TEM images and corresponding simulated images (false-colored) of bilayer moiré superlattices with a variety of twist angles. Scale bars: (a) 50 nm; (c) 30 nm; (d) 1 nm; (e) 100 nm; (f) 30 nm (top left), 5 nm^{-1} (top right), 0.5 nm^{-1} (bottom two); (h−j) 2 nm.

individual sheets and the moiré pattern. The theoretical relationship between the FFT pattern of an individual nanosheet and that of a moiré pattern is illustrated in Figure 3g inset, and accordingly, the moiré *d*-spacing can be calculated as

$$d_{\mathrm{m}}(200) = \frac{d_{\mathrm{rs}}(200)}{2\sin(\theta/2)} \tag{1}$$

where θ is the twist angle and d_{m} and d_{rs} are the (200) *d*-spacings of the moiré cell and the rock-salt cell, respectively. In addition, the moiré *d*-spacing can also be directly measured from high-resolution TEM images for a variety of twist angles, verifying the results calculated using eq 1, as plotted in Figure 3g.

Figures 3h−j and S5 show atomic-resolution TEM images and corresponding image simulations (blue images; see Supplementary Methods S2) of moiré superlattices with various twist angles. For smaller twist angles, the (quasi-)unit cell of the moiré pattern is more obvious, and the superlattice appears as an array of identical quantum dots. For example, the moiré superlattice with a 3.2° twist angle (as measured by the rotation angle of FFT spots) consists of periodic AA/AB regions arranged in square symmetry with DP regions filled in the diagonal positions (Figure 3h), resembling an epitaxially fused superlattice of 5−6 nm PbS quantum dots.[32] At a large twist angle close to 45°, the moiré superlattice resembles 2D octagonal quasicrystals (Figure 3j), showing an approximate C_8 symmetry in the TEM image and reflecting the S_8 symmetry of octagonal quasicrystals.

Structural Analysis of the Moiré Superlattice Interface. Figure 4a shows the TEM image along the basal plane (side view) of a moiré superlattice composed of three PbS sheets (labeled as S1, S2, and S3). The three sheets have a consistent thickness of approximately 3.0 nm and consist of 10 (002) planes. Neighboring sheets (S1−S2 or S2−S3) are in direct contact with an interfacial spacing of 3 Å and no trace of ligands at interface. For comparison, a bilayer with even one interfacial ligand residue would appear rather different, showing a larger interfacial distance of >5 Å (Figure S6). The clear interface between PbS sheets suggests the efficiency of the as-described ligand removal method.

Experimentally, one can evaluate whether an interface is coupled by chemical bonding or vdW interactions by measuring the interatom distance and analyzing whether there is a vdW gap (as shown in Figure S7). For example, the covalent radius of a carbon atom is 0.76 Å, and the interlayer distance of graphene is 3.46 Å; hence, the vdW gap is 1.94 Å. By contrast, the ionic radii of Pb^{2+} and S^{2-} are 1.33 and 1.84 Å,[43] respectively, giving an ionic bond length of 3.17 Å. The measured interfacial distance in PbS twisted superlattices (Figure 4c) is 3.35 Å, only slightly larger (by 0.18 Å) than the bonding length. Moreover, we performed additional DFT calculations to elucidate the metavalent/chemical bonding of Pb−S. The calculated bonding energy is around 0.28 eV/bond, which is much larger than the typical vdW interaction (usually below 0.1 eV/bond).[44] For example, the vdW interaction in graphite is about 0.03 eV/bond.[45] Therefore, we evaluate that the PbS twisted superlattices are coupled by chemical bonding. To better visualize the bonding at the interface, we also performed electron population analysis of the 3.47° twisted superlattice. As shown in Figure S8, the Bloch states of bands are connected in different layers, demonstrating the interlayer bonding directly.

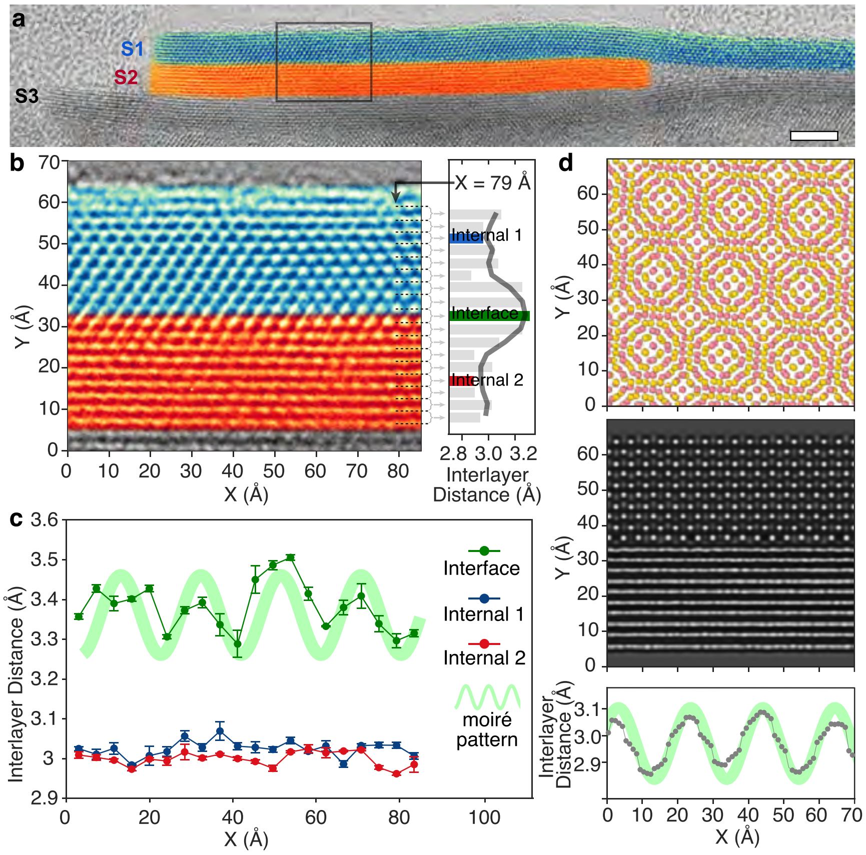

Figure 4. Structural analysis of the moiré superlattice interface. (a) Side view of a moiré superlattice composed of three sheets, S1, S2, and S3. S1 and S2 are false-colored for clarity. Scale bar, 5 nm. (b) Higher-resolution image of the boxed region in (a) and demonstration of measuring interlayer distances. The *Y* positions of the layers (marked by dashed lines) are evaluated by finding the brightest dots/strips in the image at the section with *X* = 79 Å, and the interlayer distances are calculated as the differences of neighboring Y positions (marked by brackets and arrows). Two internal interlayers in each sheet and the interface of S1 and S2 are highlighted in blue, red, and green, respectively, as representative interlayers for further analysis in (c). (c) Interlayer distance fluctuation obtained by measuring three representative interlayers at different *X* locations. Error bars indicate the standard deviation of measurements using three different sampling widths of 4, 6, and 8 Å. The thick green line shows the moiré periodicity of the bilayer superlattice with an 11.5° twist angle. (d) Theoretically optimized atomic structure (top), simulated side-view image (middle), and calculated interfacial distance fluctuation (bottom, gray dots) of an 11.5° twist superlattice. The moiré periodicity (thick green line) is shown for comparison.

Furthermore, S1 and S3 are deformed beyond the right end of S2, indicating strong interlayer metavalent interactions and large deformability of naked PbS at the sub-10 nm scale.[46] This large deformability of uncoupled nanosheets is consistent with the self-rolling behavior of individual naked nanosheets in the solution phase (Supplementary Text S2). Additionally, this also suggests that forming superlattices is an effective way to stabilize the naked nanosheets.

Further scrutiny of the side-view image in Figure 4b reveals that S1 is oriented along a [110] axis regarding the viewing direction based on the observed elongated hexagonal pattern, whereas S2 is tilted away from a low-index zone axis. This indicates that the sheets are rotated around the basal plane regarding one another, confirming the formation of moiré superlattices with direct interlayer contact. We further measured the lattice spacings in the superlattice at different *X* locations in real space based on TEM image simulations and the recognition of the image peak positions, as detailed in Supplementary Text S3. The right graph in Figure 4b shows an example at *X* = 79 Å, where the (002) spacings are approximately 3.0 Å (similar to that in the bulk crystal) for the inner layers inside each sheet but become slightly larger at the S1−S2 interface. We selected two internal interlayers in each sheet (labeled as Internal 1 and 2) and the S1−S2 interface representative interlayers and examined their interlayer spacings at different *X* locations. As shown in Figure 4c, the spacings of Internal 1 and 2 are consistent to ca. 3.0 Å with small fluctuations of less than 0.1 Å, whereas both the mean value (3.35 Å) and the fluctuations (>0.2 Å) of the interfacial spacing are considerably larger. Moreover, the fluctuation of the interfacial spacing exhibits a periodicity that matches the theoretical moiré periodicity of the bilayer superlattice with a twist angle of 11.5°. We simulated the side-view image of the theoretically optimized 11.5° twist angle superlattice and calculated the interfacial spacing in the simulated image (Figure 4d). There is indeed a considerable interfacial spacing fluctuation in the simulated image that matches the theoretical moiré periodicity. The experimental and theoretical structural analyses jointly suggest the structural reconstruction at the superlattice interface and its correlation to the moiré periodicity.

Twist-Angle-Dependent Electronic States of Moiré Superlattices. We employ monochromatized electron energy loss spectroscopy (EELS) in an aberration-corrected scanning transmission electron microscope (STEM) to investigate the electronic excitation of moiré superstructures as a function of twist angle. Because of the advantage of the latest direct detection camera and the large absorption efficiency of PbS, the low-loss spectra in the exciton region exhibit high signal-to-noise ratios (Figure S9). Figure 5a shows the overview images of two representative superlattices with twist angles of 1.3° and 3.0° and the corresponding EELS scanning profiles. Other superlattices that were measured have larger twist angles (4.6°, 12°, and 35°). Because all of the moiré superlattices were measured in one experiment with identical conditions, we can compare the thickness of individual sheets from the scattering intensity from nonoverlapping regions with only a single sheet in projection. We find that all of the individual nanosheets in the moiré superlattices have a similar thickness with less than 10% difference.

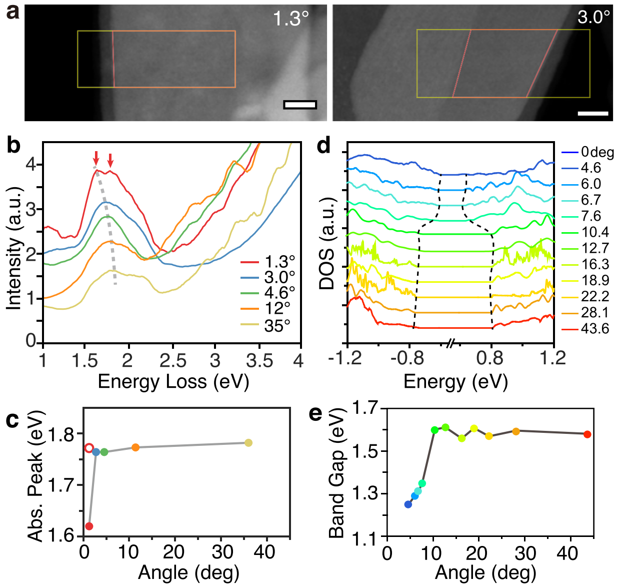

Figure 5. Twist-angle-dependent STEM-EELS analysis and electronic states of moiré superlattices. (a) Overview images of two representative superlattices with twist angles of 1.3° and 3.0°. Yellow and red boxes mark the scanning regions and bilayer regions for STEM-EELS integration, respectively. Scale bars, 20 nm. (b) Energy loss spectra of the bilayer regions of moiré superlattices with a variety of twist angles. Red arrows indicate the peak split at 1.3°. The energy dispersion of all spectra is 9 meV/pixel. (c) Change in the spectral peak with twist angle extracted from (b). Solid and open dots at 1.3° show the positions of the two split peaks. (d) Direct calculation of the densities of states of commensurate moiré superlattices with a variety of twist angles. Black dashed lines connect the positions of the first valence or conduction band for each structure. (e) Band gap change with twist angle extracted from (d).

The integrated spectra of the double-layer regions with various twist angles are plotted in Figure 5b, and the peak locations are extracted in Figure 5c. These plots show that the spectral peak slightly shifts to lower energy as the twist angle decreases from 35.3° to 3.0°, but the peak energy dramatically decreases from 3.0° to 1.3°. This sudden decrease in peak energy at 1.3° is caused by the emergent peak split (red arrows in Figure 5b) at the positions of 1.62 and 1.77 eV, corresponding to the separation of emergent flat bands in small-twist-angle superlattices as demonstrated by the DFT calculations in the next section.

Features in low-loss EEL spectra arise due to interband excitation and intraband transitions in a similar way to optical spectra,[47,48] which are qualitatively reflective of the electronic excitation or the band gap. To understand the abrupt EELS peak change at small twist angle, we performed direct self-consistent calculations by constructing large moiré unit cells (up to 4360 atoms) with commensurate angles (Supplementary Text S1). The densities of states (DOS) of the moiré cells with twist angles ranging from 4.47° to 43.6° are shown in Figure 5d, and the corresponding band gaps are plotted in Figure 5e. For superlattices with a twist angle larger than 10.4°, the band gap fluctuates around a constant. However, the band gap drops rapidly as the twist angle decreases from 10.4° to smaller angles (Figure 5e). The difference of critical angles in Figure 5c and Figure 5e is caused by two effects: (1) the necessary approximations used in the DFT method and (2) the fact that our calculations are based on thinner moiré superlattices compared to the experimental structures because of the ultralarge computational cost (up to 4360 atoms). Because the atomic relaxation in thinner twisted structures is larger than that in thicker ones, the calculated critical angle is expected to be overestimated (i.e., larger than the experimental one). Details are shown in Supplementary Text S4. Despite the quantitative offset, this calculated relationship between the band gap and twist angle, especially the sharp drop of the band gap at small angles, is in good agreement with our EELS experiments (Figure 5c). The experimental and theoretical results collectively suggest that the band structure of metavalent moiré superlattices is highly dependent on the twist angle, especially at small twist angles.

Band Structure Calculations of PbS Moiré Superlattices. In addition to the twist-angle-dependent band gap, the DFT calculations of band structures reveal the emergent separation of electronic states of superlattices at small twist angles (Figures 6a,b and S10). As the twist angle of a superlattice falls below 10°, the bands become narrower due to the quantum confinement of the moiré pattern, and bands near the Fermi level begin to separate from the deep and high-energy states. For example, in the case of 3.47°, the bands near the Fermi level, especially the conduction band, become extremely flat (Figure 6a,b). This emergent separation of electronic states is probably the reason for the observed peak split in the EELS spectrum at 1.3° (Figure 5b). Supplementary calculations (Figure S10) show that the separation of moiré bands, which reflects the modulation effect by the moiré pattern, becomes weaker as the nanosheets become thicker. This thickness dependence of the modulation indicates the value of synthesizing ultrathin free-standing nanosheets, stimulating future developments in the chemical and/or physical syntheses of ultrathin beyond-vdW nanosheets and their strongly coupled moiré superlattices.

Furthermore, these separated moiré bands at small twist angles are highly spatially localized. Figure 6d shows the corresponding wave functions of the conduction and valence bands, which are localized at AA and AB spots, respectively, with diameters of a few nanometres. This also indicates that the PbS moiré superlattice not only structurally resembles but also functionally mimics a well-arranged array of quantum dots with separate energy levels and electron orbitals. Our additional calculation (Supplementary Text S5) suggests that the strong metavalent modulation by the moiré pattern may lead to emergent optoelectronic properties in valleytronics, such as valley-dependent optical selection rules.

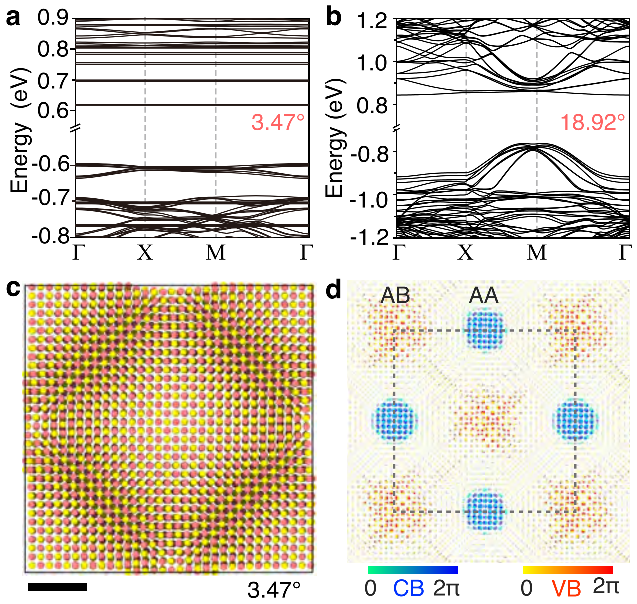

Figure 6. DFT calculations of the electronic localization. (a, b) Calculated band structures of the superlattices with twist angles of 3.47° and 18.92°. The thickness of the calculated structures is four atomic layers. The Fermi level is located at 0 eV. (c) Theoretically optimized moiré cell of the superlattice with a twist angle of 3.47°. Scale bar, 2 nm. (d) Charge densities of the valence band (VB) and conduction band (CB) of the optimized structure in (c). Color is coded by the phase of wave function, ranging from 0 to 2π. The moiré cell is marked by the dashed line.

■ CONCLUSION

We have established an approach to introduce strong metavalent interlayer interactions into moiré superlattices. Our synthesis strategy and findings on the chemically bonded moiré superlattices extend the current twistronics. Combining structural analysis, EELS measurements, and DFT calculations, we demonstrate that strong moiré modulation at small twist angles can lead to considerable structural reconstruction and electronic renormalization. This study provides a route to arrays of identical "quantum-dot" potentials by achieving deep energy modulation through metavalent interactions, providing an alternative platform for spatially variant electronic and optoelectronic properties. For instance, the strong interlayer coupling may induce a series of giant strain vortices and dipole vortices and possibly a nonlinear Hall effect. We anticipate that further experimental and theoretical studies on beyond-vdW moiré superlattices will find more types of interlayer interactions that may result in strong electronic coupling, strong correlation, and the realization of tunable emergent quantum properties.

■ ASSOCIATED CONTENT

Supporting Information

The Supporting Information is available free of charge at https://pubs.acs.org/doi/10.1021/jacs.2c09947.

> Supplementary figures, including experimental procedures, characterization data, and band structures for PbS nanosheets and superlattices; supplementary methods, including TEM imaging, EELS measurements, and theoretical calculations; and supplementary text explaining the geometry, synthetic mechanism, simulation, and valleytronic properties of PbS superlattices (PDF)

■ AUTHOR INFORMATION

Corresponding Author

Haimei Zheng − *Materials Sciences Division, Lawrence Berkeley National Laboratory, Berkeley, California 94720, United States; Department of Materials Science and Engineering, University of California, Berkeley, Berkeley, California 94720, United States;* orcid.org/0000-0003-3813-4170; Email: hmzheng@lbl.gov

Authors

Yu Wang − *Materials Sciences Division, Lawrence Berkeley National Laboratory, Berkeley, California 94720, United States; Center for Electron Microscopy and South China Advanced Institute for Soft Matter Science and Technology, School of Emergent Soft Matter, South China University of Technology, Guangzhou 510640, China;* orcid.org/0000-0002-9029-1846

Zhigang Song − *John A. Paulson School of Engineering and Applied Sciences, Harvard University, Cambridge, Massachusetts 02138, United States*

Jiawei Wan − *Materials Sciences Division, Lawrence Berkeley National Laboratory, Berkeley, California 94720, United States; Department of Materials Science and Engineering, University of California, Berkeley, Berkeley, California 94720, United States*

Sophia Betzler − *Materials Sciences Division, Lawrence Berkeley National Laboratory, Berkeley, California 94720, United States;* orcid.org/0000-0002-9163-5102

Yujun Xie − *Materials Sciences Division, Lawrence Berkeley National Laboratory, Berkeley, California 94720, United States*

Colin Ophus − *National Center for Electron Microscopy, The Molecular Foundry, Lawrence Berkeley National Laboratory, Berkeley, California 94720, United States*

Karen C. Bustillo − *National Center for Electron Microscopy, The Molecular Foundry, Lawrence Berkeley National Laboratory, Berkeley, California 94720, United States;* orcid.org/0000-0002-2096-6078

Peter Ercius − *National Center for Electron Microscopy, The Molecular Foundry, Lawrence Berkeley National Laboratory, Berkeley, California 94720, United States;* orcid.org/0000-0002-6762-9976

Lin-Wang Wang − *Materials Sciences Division, Lawrence Berkeley National Laboratory, Berkeley, California 94720, United States;* orcid.org/0000-0001-7061-2692

Complete contact information is available at: https://pubs.acs.org/10.1021/jacs.2c09947

Author Contributions

[#]Y.W. and Z.S. contributed equally.

Notes

The authors declare no competing financial interest.

■ ACKNOWLEDGMENTS

This work was supported by the U.S. Department of Energy (DOE), Office of Science, Office of Basic Energy Sciences (BES), Materials Sciences and Engineering Division, under Contract DE-AC02-05-CH11231 within the KC22ZH Program. Y.W. was partially supported by the UC Office of the

President under UC Laboratory Fees Research Program Collaborative Research and Training Award LFR-17-477148. Y.W. acknowledges the support from NSFC No.22250004 and NSF Guangdong No.2022A1515010902. Work at the Molecular Foundry was supported by DOE BES under Contract DE-AC02-05CH11231.

■ REFERENCES

(1) Cao, Y.; Fatemi, V.; Fang, S.; Watanabe, K.; Taniguchi, T.; Kaxiras, E.; Jarillo-Herrero, P. Unconventional superconductivity in magic-angle graphene superlattices. *Nature* **2018**, *556*, 43−50.

(2) Jin, C.; Regan, E. C.; Yan, A.; Utama, M. I. B.; Wang, D.; Zhao, S.; Qin, Y.; Yang, S.; Zheng, Z.; Shi, S.; Watanabe, K.; Taniguchi, T.; Tongay, S.; Zettl, A.; Wang, F. Observation of moiré excitons in WSe_2/WS_2 heterostructure superlattices. *Nature* **2019**, *567*, 76−80.

(3) Tang, Y.; Li, L.; Li, T.; Xu, Y.; Liu, S.; Barmak, K.; Watanabe, K.; Taniguchi, T.; MacDonald, A. H.; Shan, J.; et al. Simulation of Hubbard model physics in WSe_2/WS_2 moiré superlattices. *Nature* **2020**, *579*, 353−358.

(4) Lu, X.; Stepanov, P.; Yang, W.; Xie, M.; Aamir, M. A.; Das, I.; Urgell, C.; Watanabe, K.; Taniguchi, T.; Zhang, G.; et al. Superconductors, orbital magnets and correlated states in magic-angle bilayer graphene. *Nature* **2019**, *574*, 653−657.

(5) Arora, H. S.; Polski, R.; Zhang, Y.; Thomson, A.; Choi, Y.; Kim, H.; Lin, Z.; Wilson, I. Z.; Xu, X.; Chu, J.-H.; et al. Superconductivity in metallic twisted bilayer graphene stabilized by WSe_2. *Nature* **2020**, *583*, 379−384.

(6) Cao, Y.; Fatemi, V.; Demir, A.; Fang, S.; Tomarken, S. L.; Luo, J. Y.; Sanchez-Yamagishi, J. D.; Watanabe, K.; Taniguchi, T.; Kaxiras, E.; Ashoori, R. C.; Jarillo-Herrero, P. Correlated insulator behaviour at half-filling in magic-angle graphene superlattices. *Nature* **2018**, *556*, 80−84.

(7) Nuckolls, K. P.; Oh, M.; Wong, D.; Lian, B.; Watanabe, K.; Taniguchi, T.; Bernevig, B. A.; Yazdani, A. Strongly correlated Chern insulators in magic-angle twisted bilayer graphene. *Nature* **2020**, *588*, 610−615.

(8) Chen, G.; Sharpe, A. L.; Fox, E. J.; Zhang, Y.-H.; Wang, S.; Jiang, L.; Lyu, B.; Li, H.; Watanabe, K.; Taniguchi, T.; et al. Tunable correlated Chern insulator and ferromagnetism in a moiré superlattice. *Nature* **2020**, *579*, 56−61.

(9) Ribeiro-Palau, R.; Zhang, C.; Watanabe, K.; Taniguchi, T.; Hone, J.; Dean, C. R. Twistable electronics with dynamically rotatable heterostructures. *Science* **2018**, *361*, 690−693.

(10) Hu, G.; Ou, Q.; Si, G.; Wu, Y.; Wu, J.; Dai, Z.; Krasnok, A.; Mazor, Y.; Zhang, Q.; Bao, Q.; Qiu, C.-W.; Alú, A. Topological polaritons and photonic magic angles in twisted α-MoO_3 bilayers. *Nature* **2020**, *582*, 209−213.

(11) Carr, S.; Fang, S.; Kaxiras, E. Electronic-structure methods for twisted moiré layers. *Nat. Rev. Mater.* **2020**, *5*, 748−763.

(12) Dean, C. R.; Wang, L.; Maher, P.; Forsythe, C.; Ghahari, F.; Gao, Y.; Katoch, J.; Ishigami, M.; Moon, P.; Koshino, M.; et al. Hofstadter's butterfly and the fractal quantum Hall effect in moiré superlattices. *Nature* **2013**, *497*, 598−602.

(13) Jiang, Y.; Lai, X.; Watanabe, K.; Taniguchi, T.; Haule, K.; Mao, J.; Andrei, E. Y. Charge order and broken rotational symmetry in magic-angle twisted bilayer graphene. *Nature* **2019**, *573*, 91−95.

(14) Uri, A.; Grover, S.; Cao, Y.; Crosse, J. A.; Bagani, K.; Rodan-Legrain, D.; Myasoedov, Y.; Watanabe, K.; Taniguchi, T.; Moon, P.; et al. Mapping the twist-angle disorder and Landau levels in magic-angle graphene. *Nature* **2020**, *581*, 47−52.

(15) Sunku, S. S.; Ni, G. X.; Jiang, B. Y.; Yoo, H.; Sternbach, A.; McLeod, A. S.; Stauber, T.; Xiong, L.; Taniguchi, T.; Watanabe, K.; Kim, P.; Fogler, M. M.; Basov, D. N. Photonic crystals for nano-light in moiré graphene superlattices. *Science* **2018**, *362*, 1153−1156.

(16) Tran, K.; et al. Evidence for moiré excitons in van der Waals heterostructures. *Nature* **2019**, *567*, 71−75.

(17) Alexeev, E. M.; et al. Resonantly hybridized excitons in moiré superlattices in van der Waals heterostructures. *Nature* **2019**, *567*, 81−86.

(18) Seyler, K. L.; Rivera, P.; Yu, H.; Wilson, N. P.; Ray, E. L.; Mandrus, D. G.; Yan, J.; Yao, W.; Xu, X. Signatures of moiré-trapped valley excitons in $MoSe_2/WSe_2$ heterobilayers. *Nature* **2019**, *567*, 66−70.

(19) Sharpe, A. L.; Fox, E. J.; Barnard, A. W.; Finney, J.; Watanabe, K.; Taniguchi, T.; Kastner, M.; Goldhaber-Gordon, D. Emergent ferromagnetism near three-quarters filling in twisted bilayer graphene. *Science* **2019**, *365*, 605−608.

(20) Liu, Y.; Huang, Y.; Duan, X. Van der Waals integration before and beyond two-dimensional materials. *Nature* **2019**, *567*, 323−333.

(21) Sutter, P.; Wimer, S.; Sutter, E. Chiral twisted van der Waals nanowires. *Nature* **2019**, *570*, 354−357.

(22) Rhodes, D.; Chae, S. H.; Ribeiro-Palau, R.; Hone, J. Disorder in van der Waals heterostructures of 2D materials. *Nat. Mater.* **2019**, *18*, 541−549.

(23) Weston, A.; Zou, Y.; Enaldiev, V.; Summerfield, A.; Clark, N.; Zólyomi, V.; Graham, A.; Yelgel, C.; Magorrian, S.; Zhou, M.; et al. Atomic reconstruction in twisted bilayers of transition metal dichalcogenides. *Nat. Nanotechnol.* **2020**, *15*, 592−597.

(24) Dong, R.; Zhang, T.; Feng, X. Interface-assisted synthesis of 2D materials: Trend and challenges. *Chem. Rev.* **2018**, *118*, 6189−6235.

(25) Kooi, B. J.; Wuttig, M. Chalcogenides by Design: Functionality through Metavalent Bonding and Confinement. *Adv. Mater.* **2020**, *32*, 1908302.

(26) Kazmierczak, N. P.; Van Winkle, M.; Ophus, C.; Bustillo, K. C.; Carr, S.; Brown, H. G.; Ciston, J.; Taniguchi, T.; Watanabe, K.; Bediako, D. K. Strain fields in twisted bilayer graphene. *Nat. Mater.* **2021**, *20*, 956−963.

(27) Shabani, S.; Halbertal, D.; Wu, W.; Chen, M.; Liu, S.; Hone, J.; Yao, W.; Basov, D. N.; Zhu, X.; Pasupathy, A. N. Deep moiré potentials in twisted transition metal dichalcogenide bilayers. *Nat. Phys.* **2021**, *17*, 720−725.

(28) Xu, Y.; Ray, A.; Shao, Y.-T.; Jiang, S.; Lee, K.; Weber, D.; Goldberger, J. E.; Watanabe, K.; Taniguchi, T.; Muller, D. A.; et al. Coexisting ferromagnetic−antiferromagnetic state in twisted bilayer CrI_3. *Nat. Nanotechnol.* **2022**, *17*, 143−147.

(29) Kennes, D. M.; Claassen, M.; Xian, L.; Georges, A.; Millis, A. J.; Hone, J.; Dean, C. R.; Basov, D.; Pasupathy, A. N.; Rubio, A. Moiré heterostructures as a condensed-matter quantum simulator. *Nat. Phys.* **2021**, *17*, 155−163.

(30) Song, Z.; Sun, X.; Wang, L. Switchable Asymmetric Moiré Patterns with Strongly Localized States. *J. Phys. Chem. Lett.* **2020**, *11*, 9224−9229.

(31) Zhang, C.; Chuu, C.-P.; Ren, X.; Li, M.-Y.; Li, L.-J.; Jin, C.; Chou, M.-Y.; Shih, C.-K. Interlayer couplings, Moiré patterns, and 2D electronic superlattices in MoS_2/WSe_2 hetero-bilayers. *Sci. Adv.* **2017**, 3, No. e1601459.

(32) Whitham, K.; Yang, J.; Savitzky, B. H.; Kourkoutis, L. F.; Wise, F.; Hanrath, T. Charge transport and localization in atomically coherent quantum dot solids. *Nat. Mater.* **2016**, *15*, 557−563.

(33) Wigner, E. Effects of the electron interaction on the energy levels of electrons in metals. *Trans. Faraday Soc.* **1938**, *34*, 678−685.

(34) Li, H.; Li, S.; Regan, E. C.; Wang, D.; Zhao, W.; Kahn, S.; Yumigeta, K.; Blei, M.; Taniguchi, T.; Watanabe, K.; et al. Imaging two-dimensional generalized Wigner crystals. *Nature* **2021**, *597*, 650−654.

(35) Regan, E. C.; Wang, D.; Jin, C.; Bakti Utama, M. I.; Gao, B.; Wei, X.; Zhao, S.; Zhao, W.; Zhang, Z.; Yumigeta, K.; et al. Mott and generalized Wigner crystal states in WSe_2/WS_2 moiré superlattices. *Nature* **2020**, *579*, 359−363.

(36) Naguib, M.; Mochalin, V. N.; Barsoum, M. W.; Gogotsi, Y. 25th anniversary article: MXenes: a new family of two-dimensional materials. *Adv. Mater.* **2014**, *26*, 992−1005.

(37) Ji, D.; Cai, S.; Paudel, T. R.; Sun, H.; Zhang, C.; Han, L.; Wei, Y.; Zang, Y.; Gu, M.; Zhang, Y.; et al. Freestanding crystalline oxide perovskites down to the monolayer limit. *Nature* **2019**, *570*, 87−90.

(38) Wu, M.; Wang, Z.; Liu, J.; Li, W.; Fu, H.; Sun, L.; Liu, X.; Pan, M.; Weng, H.; Dincă, M.; et al. Conetronics in 2D metal-organic frameworks: double/half Dirac cones and quantum anomalous Hall effect. *2D Mater.* **2017**, *4*, 015015.

(39) Halbertal, D.; Finney, N. R.; Sunku, S. S.; Kerelsky, A.; Rubio-Verdú, C.; Shabani, S.; Xian, L.; Carr, S.; Chen, S.; Zhang, C.; et al. Moiré metrology of energy landscapes in van der Waals heterostructures. *Nat. Commun.* **2021**, *12*, 242.

(40) Coropceanu, I.; Janke, E. M.; Portner, J.; Haubold, D.; Nguyen, T. D.; Das, A.; Tanner, C. P.; Utterback, J. K.; Teitelbaum, S. W.; Hudson, M. H.; et al. Self-assembly of nanocrystals into strongly electronically coupled all-inorganic supercrystals. *Science* **2022**, *375*, 1422−1426.

(41) Schliehe, C.; Juarez, B. H.; Pelletier, M.; Jander, S.; Greshnykh, D.; Nagel, M.; Meyer, A.; Foerster, S.; Kornowski, A.; Klinke, C.; et al. Ultrathin PbS sheets by two-dimensional oriented attachment. *Science* **2010**, *329*, 550−553.

(42) Zhang, C.; Wang, B.; Li, W.; Huang, S.; Kong, L.; Li, Z.; Li, L. Conversion of invisible metal-organic frameworks to luminescent perovskite nanocrystals for confidential information encryption and decryption. *Nat. Commun.* **2017**, *8*, 1138.

(43) Cordero, B.; Gómez, V.; Platero-Prats, A. E.; Revés, M.; Echeverría, J.; Cremades, E.; Barragán, F.; Alvarez, S. Covalent radii revisited. *Dalton Trans* **2008**, 2832−2838.

(44) Lee, K.; Murray, É. D.; Kong, L.; Lundqvist, B. I.; Langreth, D. C. Higher-accuracy van der Waals density functional. *Phys. Rev. B* **2010**, *82*, 081101.

(45) Chakarova-Käck, S. D.; Schröder, E.; Lundqvist, B. I.; Langreth, D. C. Application of van der Waals density functional to an extended system: Adsorption of benzene and naphthalene on graphite. *Phys. Rev. Lett.* **2006**, *96*, 146107.

(46) Wang, Y.; Peng, X.; Abelson, A.; Xiao, P.; Qian, C.; Yu, L.; Ophus, C.; Ercius, P.; Wang, L.-W.; Law, M.; et al. Dynamic deformability of individual PbSe nanocrystals during superlattice phase transitions. *Sci. Adv.* **2019**, *5*, No. eaaw5623.

(47) Hage, F. S.; Nicholls, R. J.; Yates, J. R.; McCulloch, D. G.; Lovejoy, T. C.; Dellby, N.; Krivanek, O. L.; Refson, K.; Ramasse, Q. M. Nanoscale momentum-resolved vibrational spectroscopy. *Sci. Adv.* **2018**, *4*, No. eaar7495.

(48) Gogoi, P. K.; Lin, Y.-C.; Senga, R.; Komsa, H.-P.; Wong, S. L.; Chi, D.; Krasheninnikov, A. V.; Li, L.-J.; Breese, M. B.; Pennycook, S. J.; et al. Layer rotation-angle-dependent excitonic absorption in van der Waals heterostructures revealed by electron energy loss spectroscopy. *ACS Nano* **2019**, *13*, 9541−9550.